Electronic supplementary information for

Ordered Grain Boundary Reconstruction Induces High-Efficiency Thermoelectric Power Generation in SnTe

Qian Deng, [‡,a] Fujie Zhang, [‡,a] Xiaoyu Yang, [‡,b] Ruiheng Li, [a] Chengliang Xia, [c] Pengfei Nan, [*,b] Yue Chen, [c] Binghui Ge, [b] Ran Ang, [*,a,d] and Jiaqing He, [*,e,f]

[a]Key Laboratory of Radiation Physics and Technology, Ministry of Education, Institute of Nuclear Science and Technology, Sichuan University, Chengdu 610064, China

[b]Information Materials and Intelligent Sensing Laboratory of Anhui Province, Leibniz International Joint Research Center of Materials Sciences of Anhui Province, Institutes of Physical Science and Information Technology, Anhui University, Hefei, 230601, China

[c]Department of Mechanical Engineering, The University of Hong Kong, Pokfulam Road, Hong Kong SAR, China

[d]Institute of New Energy and Low-Carbon Technology, Sichuan University, Chengdu 610065, China

[e]Shenzhen Key Laboratory of Thermoelectric Materials, Department of Physics, Southern University of Science and Technology, Shenzhen 518055, China

[f]Guangdong Provincial Key Laboratory of Advanced Thermoelectric Materials and Device Physics, Southern University of Science and Technology, Shenzhen 518055, China.

‡Q. D., F. Z and X. Y. contributed equally to this work.

*Correspondence and requests for materials should be addressed to J.Q.H (e-mail: hejq@sustech.edu.cn), R.A. (e-mail: rang@scu.edu.cn), and P.F.N. (e-mail: npf@ahu.edu.cn).

Experimental section

Material characterization and module testing

Thermal conductivity (κ_t) was calculated as $\kappa_t = dC_pD$, where D is the thermal diffusivity measured by a laser flash technique with the Netzsch LFA467 system, and C_p is the heat capacity estimated by $C_p(k_B/\text{atom}) = 3.07 + 4.7(T/\text{K} - 300)/10000$.[1,2] Ignoring the bipolar thermal conductivity (κ_{bip}), lattice thermal conductivity (κ_l) was directly obtained by subtracting electronic conductivity (κ_e), calculated using the Wiedemann-Franz relationship, $\kappa_e = LT/\rho$, where L is the Lorentz number.[3] L was derived using the single parabolic band (SPB) model.[4]

Electronic band structure calculations

We employed the Korringa-Kohn-Rostoker (KKR) method and the coherent potential approximation (CPA) within the AkaiKKR (Machikaneyama) package to calculate the electronic band structures and densities of states (DOS) of SnTe, $SnSb_{0.16}Te_{1.24}$, and $Sn_{0.88}Mn_{0.12}Sb_{0.16}Te_{1.24}$.[5,6] The exchange-correlation energy was parameterized using the Moruzzi, Janak, and Williams form,[7] and spin-orbit interaction was included. Dense meshes with 2858, 4542, and 4242 k-points were utilized for self-consistent calculations of electronic band structure and DOS, respectively. Magnetic calculations were conducted for $Sn_{0.88}Mn_{0.12}Sb_{0.16}Te_{1.24}$. Experimental lattice constants of SnTe, $SnSb_{0.16}Te_{1.24}$, and $Sn_{0.88}Mn_{0.12}Sb_{0.16}Te_{1.24}$ were used in our calculations: 6.320 Å, 6.278 Å, and 6.239 Å, respectively.

Modeling study on electronic transport

The single parabolic (SPB) model[8]

The Seebeck coefficient S:

$$S = \frac{k_b}{e}\left[\frac{(r+5/2)F_{r+3/2}(\eta)}{(r+3/2)F_{r+1/2}(\eta)} - \eta\right]$$

(S1)

where η is the reduced chemical potential, k_b is the Boltzmann constant, e is the electron charge, and r is the scattering factor.

The carrier concentration n_H:

$$n_H = 4\pi\left[\frac{2m^*k_BT}{h^2}\right]^{3/2} F_{1/2}$$

(S2)

where m^* is the effective mass of the density of states, accounting for band degeneracy, h is the Plank constant, and T is the absolute temperature.

The mobility μ_H:

$$\mu_H = \mu_0\frac{F_{-1/2}}{2F_0} = \frac{\tau_0 e}{m^*}\frac{F_{-1/2}}{2F_0}$$

(S3)

where τ_0 is the relaxation time closely related to the energy in the case of acoustic phonon scattering: $\tau_0 = \dfrac{h^4 C_l}{8\sqrt{2}\pi^3 E_{def}^2 m^* kT^{3/2}}$.[9] Here, C_l is a parameter determined by the combination of elastic constants,[10] and E_{def} is a combination of deformation potentials for multivalley systems.[11]

The Hall factor A:

$$A = \frac{3}{2}F_{1/2}(\eta)\frac{F_{-1/2}}{2F_0^2}$$

(S4)

The Hall factor reflects the energy scattering mechanism and the anisotropy of the energy band. In the SPB model, anisotropy does not need to be considered.

The Lorenz number L:

$$L = \frac{\kappa_B^2}{e^2}\frac{3F_0F_2 - 4F_1^2}{F_0^2}$$

(S5)

In the equations above the integral F_j is defined by

$$F_j(\eta) = \int_0^\infty \frac{\xi^j d\xi}{1 + e^{(\xi - \eta)}}$$

(S6)

The single Kane band (SKB) model

Assuming the light band is nonparabolic and the heavy band is parabolic, the SKB model and SPB model are applied to the light band and heavy band, respectively. It should be noted that the rigid band approximation is adopted, which assumes that changes in carrier concentration only adjust the position of the chemical potential and not the shape or position of the bands.[8]

As for the SKB model:[4,12,13]

The Seebeck coefficient S:

$$S = \frac{k_B}{e}\left[\frac{F_{1,-2}^1}{F_{1,-2}^0} - \eta\right]$$

(S7)

The carrier concentration n_H:

$$n_H = \frac{1}{3\pi}\left[\frac{8m^* k_B T}{h^2}\right]^{3/2} F_{3/2,0}^0$$

(S8)

The mobility μ_H:

$$\mu_H = \frac{h^4 e C_{ll}}{8\pi^3 m_I^* (2m_b^* k_B T)^{3/2} E_{def}^2 F_{3/2,0}^0} \cdot \frac{3F_{1,-2}^0}{}$$

(S9)

Due to the anisotropy of both conduction and valence bands, the inertial effective mass m_I^* and the density of states effective mass m^* are governed by the effective band mass of a single pocket along two directions $m_{//}^*$ and $m_\perp^*$:[14]

$$m^* = N_V^{2/3} m_b^* = N_V^{\frac{2}{3}}(m_\perp^{*2} m_\parallel^{*2})^{1/3}; \quad m_I^* = 3\left(\frac{2}{m_\perp^*} + \frac{1}{m_\parallel^*}\right)^{-1}.$$

(S10)

where N_V is the band degeneracy (N_{V1}=4 for the light-mass valence band, N_{V2}=12 for the heavy-mass valence band of SnTe.[15]

The Hall factor A:

$$A = \frac{3K(K+2)F_{1/2,-4}^{0}F_{3/2,0}^{0}}{(2K+1)^2 \ (F_{1,-2}^{0})^2} \tag{S11}$$

where $K = m_{\parallel}^{*}/m_{\perp}^{*}$ ($K=4$, assumed T independent), which reflects the anisotropy of the energy band.[11]

The Lorenz number L:

$$L = (\frac{k_B}{e})^2 [\frac{F_{1,-2}^{2}}{F_{1,-2}^{0}} - \left|\frac{F_{1,-2}^{1}}{F_{1,-2}^{0}}\right|^2] \tag{S12}$$

In the equations above the integral $F_{m,n}^{l}$ is defined by

$$F_{m,n}^{1} = \int_{0}^{\infty}\left(-\frac{\partial f}{\partial \varepsilon}\right)\varepsilon^{l}(\varepsilon + \beta\varepsilon^2)^{m}[(1 + 2\beta\varepsilon)^2 + 2]^{1/2}d\varepsilon \tag{S13}$$

where $\beta = \dfrac{k_B T}{E_g}$ (E_g is the band gap) is the reciprocal reduced band gap, and ε is the nonparabolicity parameter.

The two valence bands (TVB) model

It should be noted that the relative positions of the Fermi level and the two valence bands need to be considered when using the TVB model. Specifically, the difference between the reduced chemical potentials corresponding to the TVB $\Delta = \dfrac{\Delta E}{k_B T}$.[4,13] And the total electrical conductivity:

$$\sigma = \sigma_L + \sigma_\Sigma \tag{S14}$$

The total Seebeck coefficient:

$$S = \frac{S_L \sigma_L + S_\Sigma \sigma_\Sigma}{\sigma_L + \sigma_\Sigma} \tag{S15}$$

The total Lorenz number:

$$L = \frac{L_L \sigma_L + L_\Sigma \sigma_\Sigma}{\sigma_L + \sigma_\Sigma} \tag{S16}$$

The total carrier concentration n_H:

$$n_H = \frac{[bn_{LH} + n_{\Sigma H}]^2}{A_{LH}b^2 n_{LH} + A_{\Sigma H}n_{\Sigma H}}$$

(S17)

where $b=4$, that is suitable for the PbTe/SnTe system.

The total Hall coefficient R_H:

$$R_H = \frac{\sigma_L^2 R_{LH} + \sigma_\Sigma^2 R_{\Sigma H}}{(\sigma_L + \sigma_\Sigma)^2}$$

(S18)

The total Hall mobility μ_H:

$$\mu_H = R_H \sigma$$

(S19)

Debye-Callaway Model Simulation

According to the Debye-Callaway model,[16,17] κ_l can be calculated as:

$$\kappa_l = \frac{K_B}{2\pi^2\upsilon}\left(\frac{K_B}{\hbar}\right)^3 \int_0^{\Theta/T} \tau(x)\frac{x^4 e^x}{(e^x - 1)^2}dx$$

(S20)

where the integrand combined with the coefficient of the above equation represents the spectral lattice thermal conductivity (κ_s),[18,19] can be given by:

$$\kappa_s = \frac{k_B}{2\pi^2\upsilon}\left(\frac{k_B}{\hbar}\right)^3 \tau(x)\frac{x^4 e^x}{(e^x - 1)^2}$$

(S21)

Here, $v = 3^{1/3}(v_l^{-3} + 2v_t^{-3})^{-1/3}$ (v_l and v_t denote the transverse and longitudinal sound velocities, respectively) is the average speed of phonon, $x = \hbar\omega/k_B T$ (with ω denoting the phonon frequency) represents the reduced phonon frequency, Θ is Debye temperature, $\hbar$ is the reduced Planck constant, k_B is the Boltzmann constant, and τ_{tot} is the total relaxation time defined by Matthiessen's equation as: $\tau_{tot}^{-1} = \tau_U^{-1} + \tau_N^{-1} + \tau_{PD}^{-1} + \tau_D^{-1} + \tau_{GB}^{-1}$. The phonon scattering mechanisms include Umkalapp (U) phonon scattering, normal process (N), point defects (PD), nanoprecipitates (NP), dislocation (DS), and grain boundaries (GB). The respective phonon relaxation times are given by:

Umklapp and Normal process phonon scattering:

$$\tau_U^{-1} = \frac{\hbar\omega^2\gamma^2 T}{Mv^2\Theta}e^{-\Theta/T}$$

(S22)

$$\tau_N^{-1} = \beta\tau_U^{-1}$$

(S23)

where M is the average atomic mass, γ is the Grüneisen parameter, and β is the ratio between normal process and Umklapp phonon scattering.

Point defect phonon scattering:

$$\tau_{PD}^{-1} = \frac{V_0}{4\pi^2\upsilon}\Gamma\omega^4$$

(S24)

where V_0 is the average atomic volume, and Γ is the point defect scattering parameter. Disorder scattering parameter Γ are derived from the Slack and Abeles models,

assuming $\Gamma = \Gamma_M + \Gamma_{S}$,[20,21] where the scattering parameters Γ_M and Γ_S are due to mass and strain field fluctuations, respectively. The mass and strain fluctuation scattering parameter is given by:

$$\Gamma_M = \frac{\sum_{i=1}^{n} c_j (\bar{M}_i/\bar{\bar{M}})^2 f_i^1 f_i^2 [(M_i^1 - M_i^2)/\bar{M}_i]^2}{\sum_{i=1}^{n} c_i} \tag{S25}$$

$$\Gamma_S = \frac{\sum_{i=1}^{n} c_j (\bar{M}_i/\bar{\bar{M}})^2 f_i^1 f_i^2 \varepsilon [(r_i^1 - r_i^2)/\bar{r}_i]^2}{\sum_{i=1}^{n} c_i} \tag{S26}$$

where n, c_j, $\bar{M}_i$, $\bar{\bar{M}}$, M_i^k, r_i^k, f_i^k and ε are the number of sublattice, relative degeneracies, average atomic masses, average atomic mass of the compound, atomic mass of the k_{th} atom of the i_{th} sublattice, the atomic radius of the k_{th} atom of i_{th} sublattice, fractional concentrations of k_{th} atom of the i_{th} sublattice, and lattice inharmonic parameter, respectively. In particular, the mass of the Sn vacancy is estimated to be 0, and its radius is 0.5-0.6 times the ionic radius of Sn.

Nanoprecipitates scattering:

$$\tau_P^{-1} = v \left((2\pi R^2)^{-1} + \left(\frac{4}{9} \pi R^2 \left(\frac{\Delta D}{D} \right)^2 \left(\frac{\omega R}{v} \right)^4 \right)^{-1} \right)^{-1} N_p \tag{S27}$$

where R and D are the average radius and density of nanoprecipitates, respectively, and ΔD is the density difference between the precipitated phase and the matrix material, and N_P is the density of nanoprecipitates.

Dislocation scattering:

$$\tau_D^{-1} = N_D \frac{V_0^{4/3}}{v^2} \omega^3 + 0.06 N_D \gamma^2 B_D^2 \omega \left\{ \frac{1}{2} + \frac{1}{24} \left(\frac{1-2r}{1-r} \right)^2 \left[1 + \sqrt{2} \left(\frac{v_L}{v_T} \right)^2 \right]^2 \right\} \tag{S28}$$

where N_D is the number of dislocations crossing a unit length, B_D is the magnitude of the Burgers vector of the dislocation, and r is the Poisson's ratio.

Grain boundary scattering:

$$\tau_{GB}^{-1} = \frac{v_s}{l} \tag{S29}$$

where v_s is the average sound velocity, and l is the average grain size in the material.

Prediction of conversion efficiency

Based on the Seebeck effect, when there is a temperature difference $\Delta T = T_h - T_c$ between the upper and lower ends of the thermoelectric device at T_h and T_c, the open circuit voltage V_{oc} generated in the circuit is given by:

$$V_{oc} = \int_{T_c}^{T_h} S_{pn}(T)dT = S_{pn}(T)(T_h - T_c) \tag{S30}$$

where S_{pn} is the average Seebeck coefficient of a pair of p/n-materials, estimated as $S_p - S_n$.[22]

Ignoring the surface effects of each unit of the device, the internal resistance R_{in} of the device can be approximated as the sum of the resistance values of the thermoelectric materials:

$$R = N(R_p + R_n) = N\left(\int_0^H \frac{\rho_p(T)}{A_P}dx + \int_0^H \frac{\rho_n(T)}{A_n}dx\right) \tag{S31}$$

where N is the number of couples, H is the height of the thermoelectric legs, A_p is the cross-sectional area of the p-type leg, A_n is cross-sectional area of the n-type leg, ρ_p is the resistivity of the p-type material, and ρ_n is the resistivity of the n-type material.

Assuming the device load resistance R_{out}, the effective output voltage V_{out} and loop current of the device are respectively:

$$V_{out} = \frac{V_{oc}}{R + R_{out}}R_{out} \tag{S32}$$

$$I = \frac{V_{oc}}{R + R_{out}} \tag{S33}$$

The output power P is given by:

$$P = V_{out}I = \frac{S_{pn}^2(T)(T_h - T_c)^2 R_{out}}{(R + R_{out})^2} \tag{S34}$$

The maximum output power P_{max} occurs when the internal resistance of the thermoelectric device equals the resistance of the load:

$$P_{max} = \frac{S_{pn}^2(T_h - T_c)^2}{4R} \tag{S35}$$

The open-circuit heat-flow Q_{oc} of the module is:

$$Q_{oc} = N(\frac{A_P}{H}\bar{\kappa}_p + \frac{A_n}{H}\bar{\kappa}_n)\Delta T$$

(S36)

where κ_p and κ_n are the average thermal conductivity of the p-type and n-type materials, respectively.

The input heat at the hot-side Q_{in} of the module is:

$$Q_{in} = Q_{oc} - \frac{R_{out}I^2 + N(\beta_p - \beta_n)T_hI}{2} + N[S_p(T_h) - S_n(T_h)]T_hI$$

(S37)

$$\beta_p = \frac{T_c}{T_h}[\bar{S}_p - S_p(T_c)] + [S_p(T_h) - \bar{S}_p]$$

(S38)

$$\beta_n = \frac{T_c}{T_h}[S_n(T_c) - \bar{S}_n] + [\bar{S}_n - S_n(T_h)]$$

(S39)

where β_p and β_n are the combined coefficient of p-type and n-type materials, respectively. The conversion efficiency η of the module can be estimated by:

$$\eta = \frac{P}{Q_{in}}$$

(S40)

Supplementary Figures
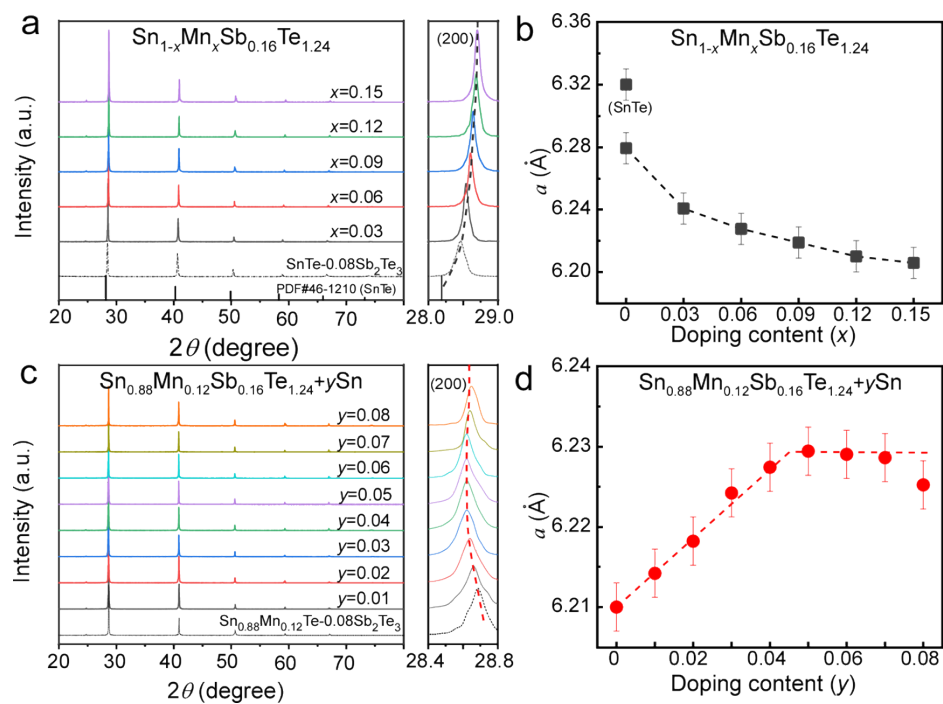
Fig. S1 Powder XRD patterns for (a) $Sn_{1-x}Mn_xSb_{0.16}Te_{1.24}$ and (c) $Sn_{0.88}Mn_{0.12}Sb_{0.16}Te_{1.24}+y$Sn, with an enlarged view of the (200) Bragg peak showing the shift. Variation of the lattice parameter a with doping levels (b) x and (d) y.
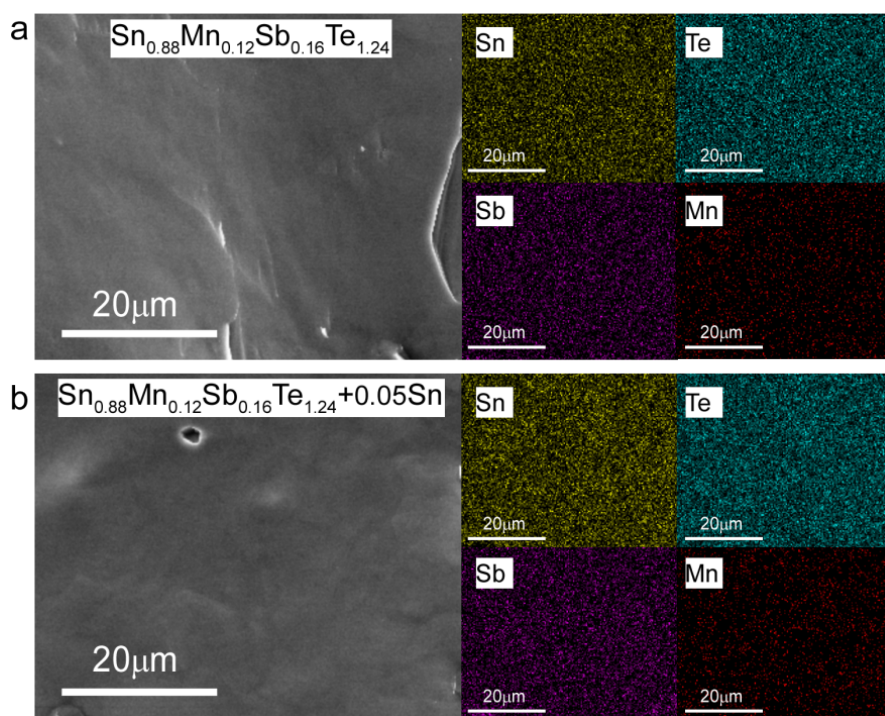
Fig. S2 Fracture SEM images and corresponding EDS elemental mappings of (a) $Sn_{0.88}Mn_{0.12}Sb_{0.16}Te_{1.24}$ and (b) $Sn_{0.88}Mn_{0.12}Sb_{0.16}Te_{1.24}+0.05Sn$.
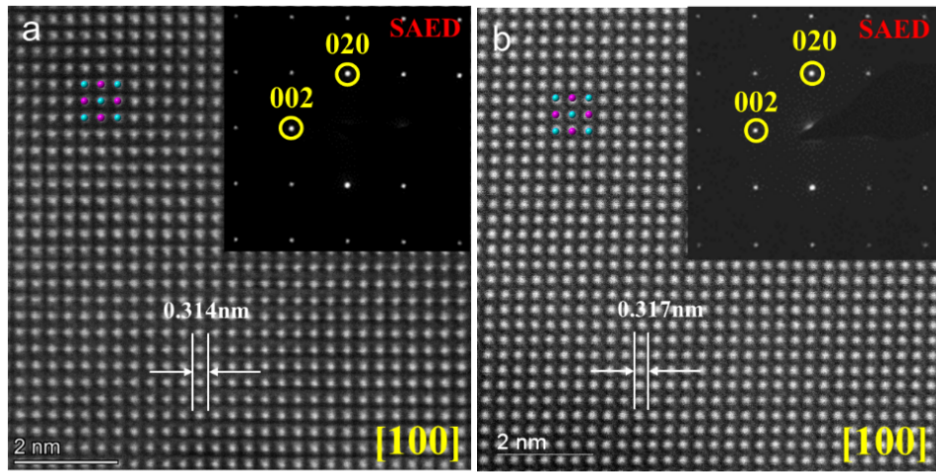
Fig. S3 Atomic resolution HADDF-STEM images of the uniform matrix for (a) $Sn_{0.88}Mn_{0.12}Sb_{0.16}Te_{1.24}$ and (b) $Sn_{0.88}Mn_{0.12}Sb_{0.16}Te_{1.24}$+0.05Sn. The insets show selected area electron diffraction (SAED) patterns of the corresponding regions.
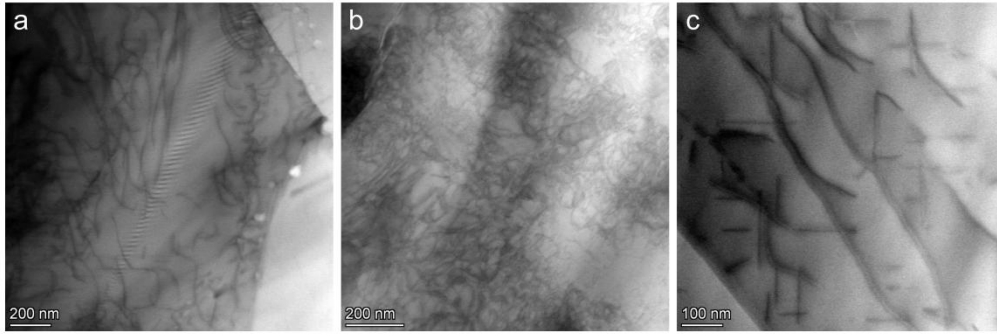
Fig. S4 Densed dislocations were uniformly distributed throughout the $Sn_{0.88}Mn_{0.12}Sb_{0.16}Te_{1.24}$ sample.
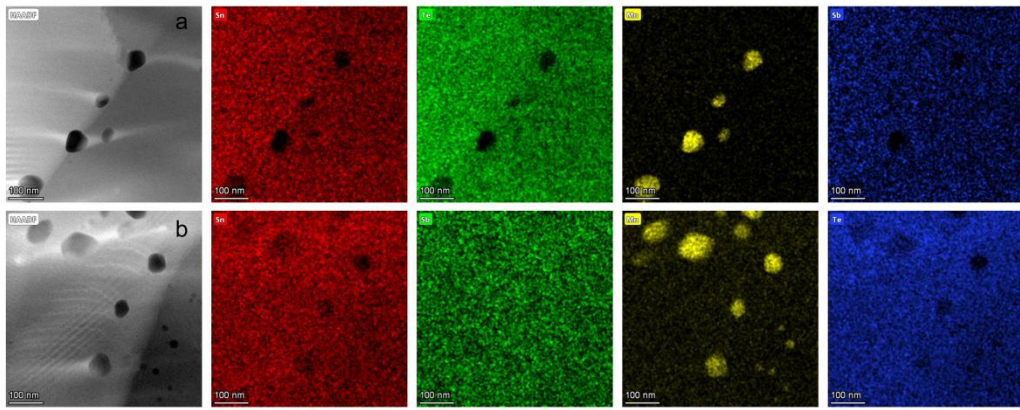
Fig. S5 HAADF-STEM images and corresponding EDS mapping of representative nanoprecipitates on the grain boundaries of the $Sn_{0.88}Mn_{0.12}Sb_{0.16}Te_{1.24}$+0.05Sn sample.
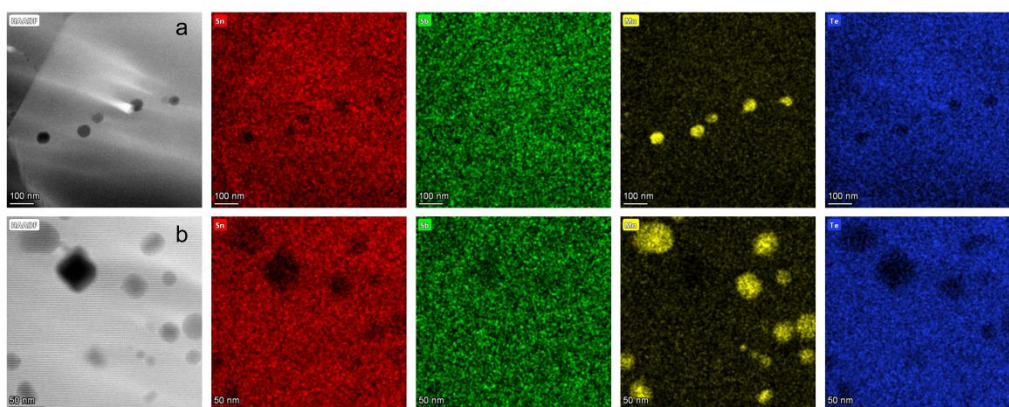
Fig. S6 HAADF-STEM image and corresponding EDS mapping of representative nanoprecipitates in the matrix of the $Sn_{0.88}Mn_{0.12}Sb_{0.16}Te_{1.24}$ sample.
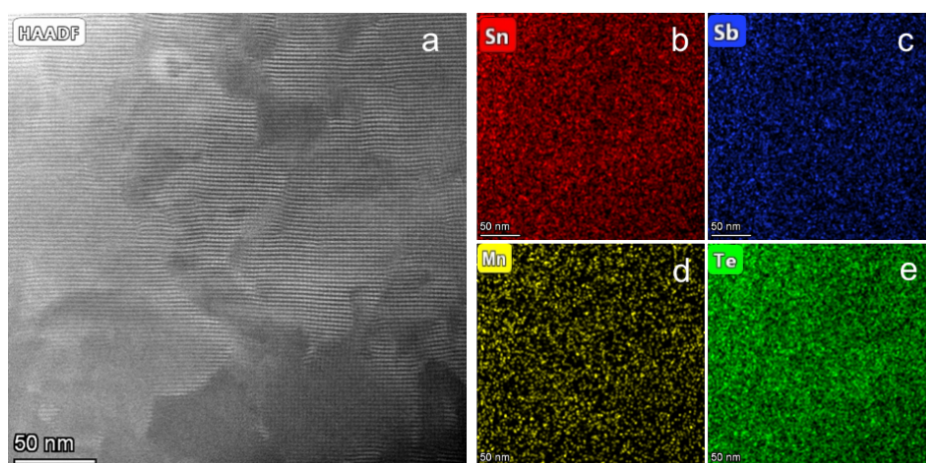
Fig. S7 (a) High-magnification HAADF-STEM image showing dense dislocations. (b–e) EDS mappings taken from (a).
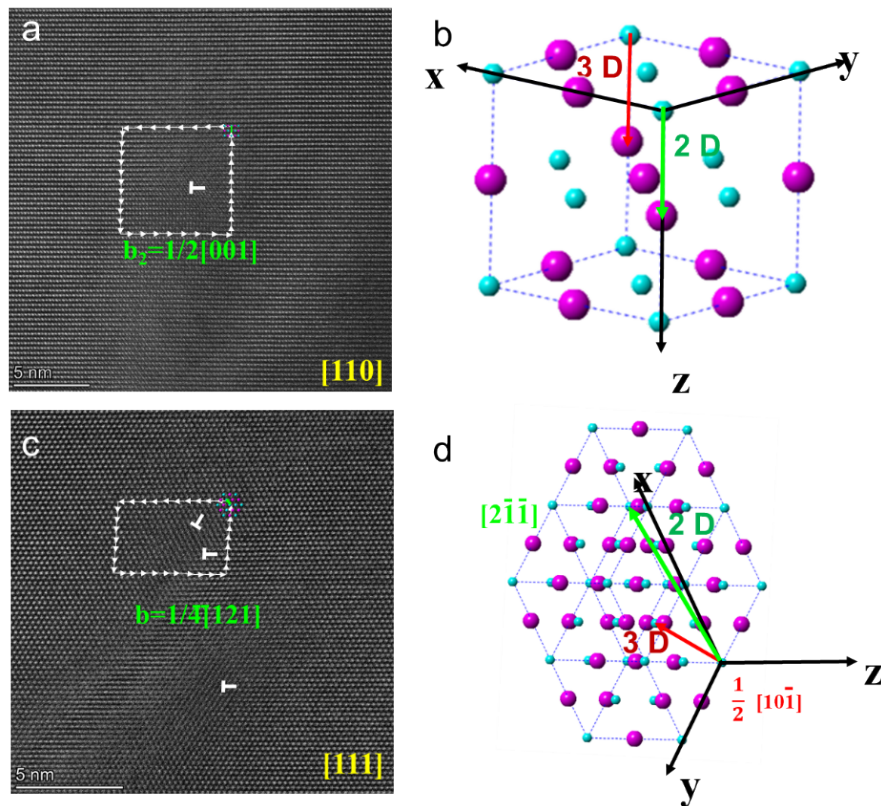
Fig. S8 Atomic resolution HAADF-STEM images showing the disappearance region of dislocation lines under (a) [110] and (c) [111] orientations, with the projected Burgers vector of the dislocation obtained by drawing the Burgers loop. (b, d) Two-dimensional projected Burgers vector of the [100] orientation corresponding to the three-dimensional 1/2[110] direction in space.
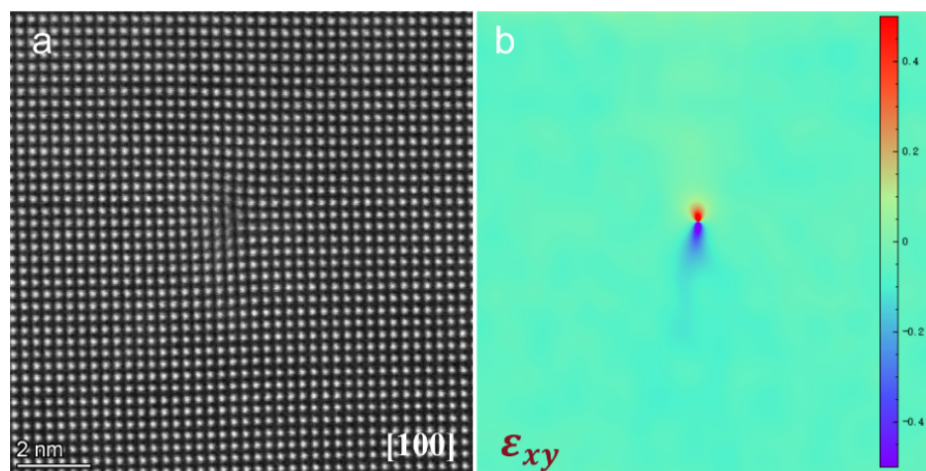
Fig. S9 (a) High-resolution HADDF-STEM image of a typical edge dislocation, and (b) corresponding GPA strain analysis.
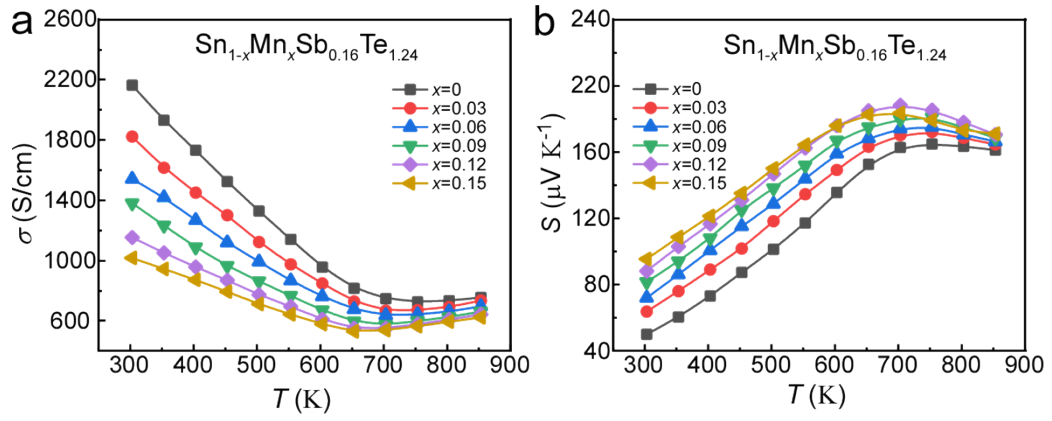
Fig. S10 (a) Temperature-dependent electrical conductivity σ, (b) Seebeck coefficient S for $Sn_{1-x}Mn_xSb_{0.16}Te_{1.24}$ (x=0-0.15) samples.
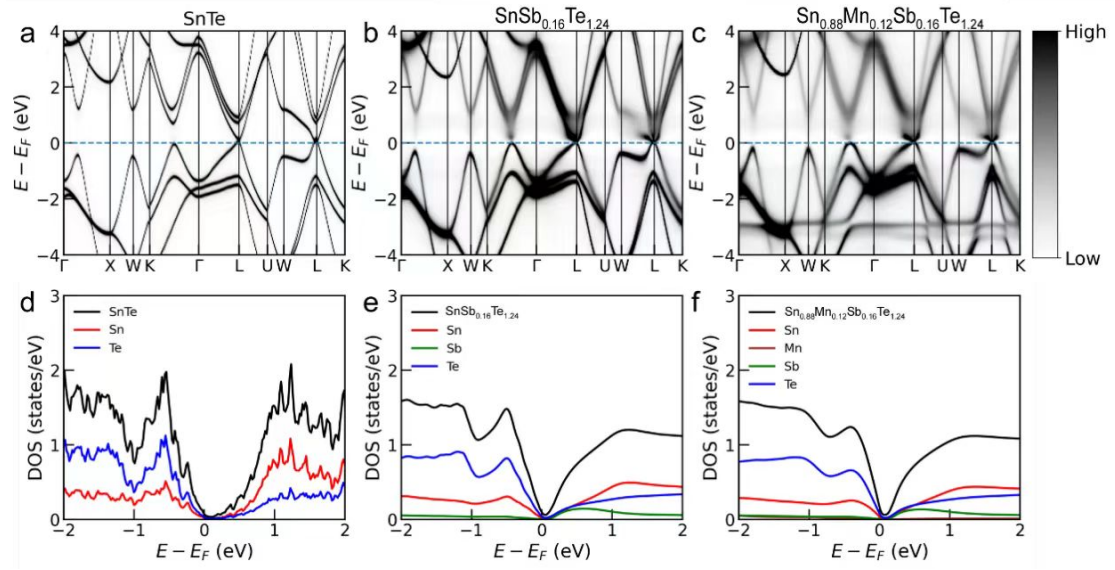
Fig. S11 Band structures and projected density of states (DOS) for (a, d) SnTe, (b, e) $SnSb_{0.16}Te_{1.24}$, and (c, f) $Sn_{0.88}Mn_{0.12}Sb_{0.16}Te_{1.24}$, calculated using the KKR-CPA method.
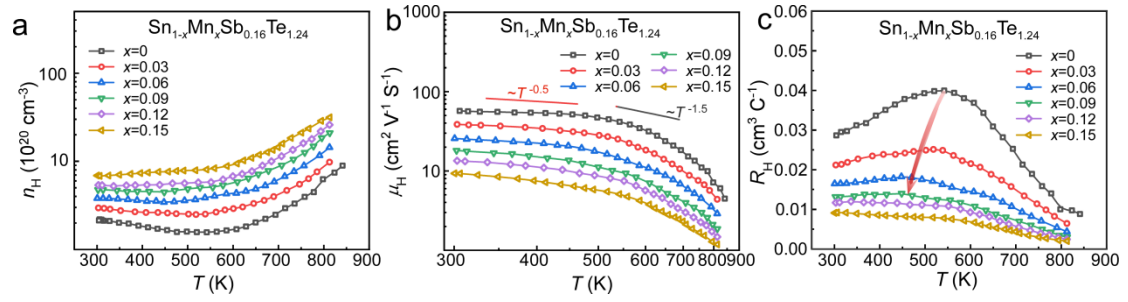
Fig. S12 (a) Temperature-dependent Carrier concentration n_H, (b) Hall mobility μ_H and (c) Hall coefficient R_H for $Sn_{1-x}Mn_xSb_{0.16}Te_{1.24}$ (x=0-0.15) samples.
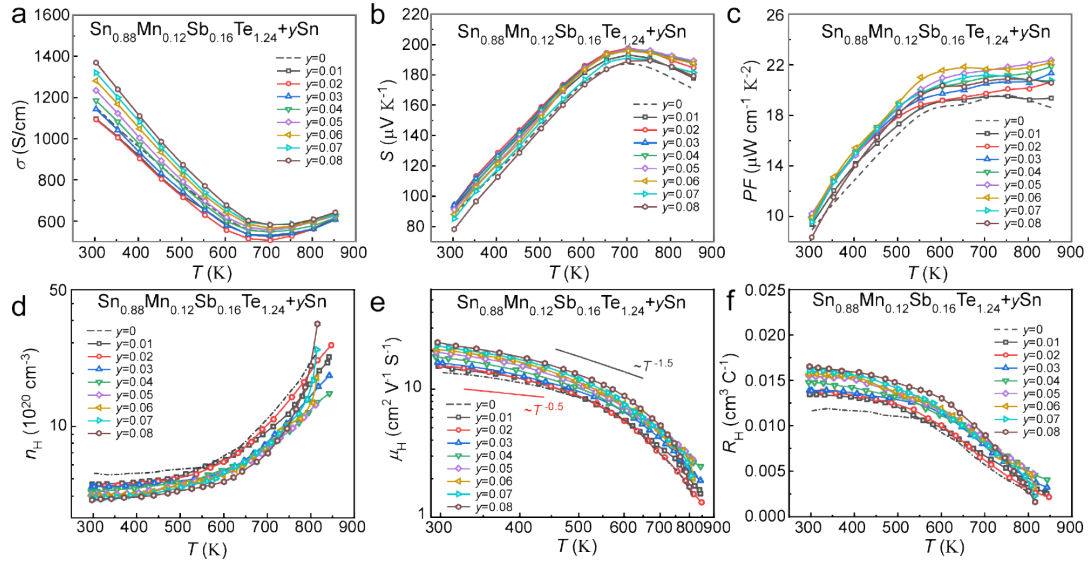
Fig. S13 (a) Temperature-dependent electrical conductivity σ, (b) Seebeck coefficient S, (c) Power factor PF, (d) Carrier concentration n_H, (e) Hall mobility μ_H and (f) Hall coefficient R_H for $Sn_{0.88}Mn_{0.12}Sb_{0.16}Te_{1.24}+ySn$ (y=0-0.08) samples.
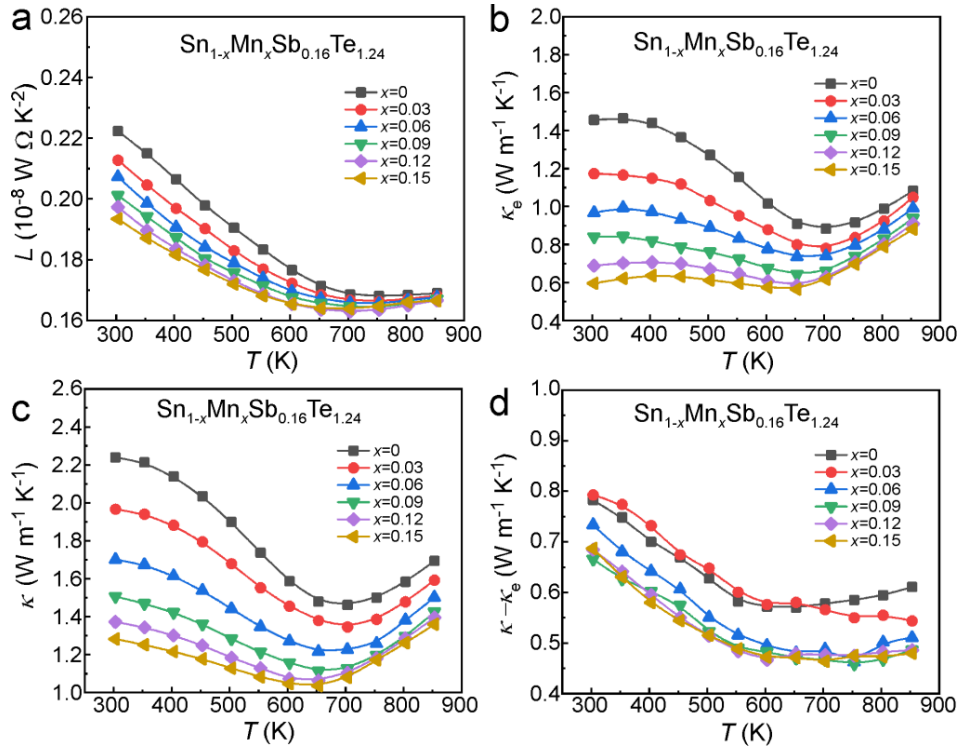
Fig. S14 Temperature-dependent (a) Lorenz number L, (b) electronic thermal conductivity κ_e, (c) total thermal conductivity κ, and (d) lattice thermal conductivity κ_l for $Sn_{1-x}Mn_xSb_{0.16}Te_{1.24}$ (x=0-0.15) samples.
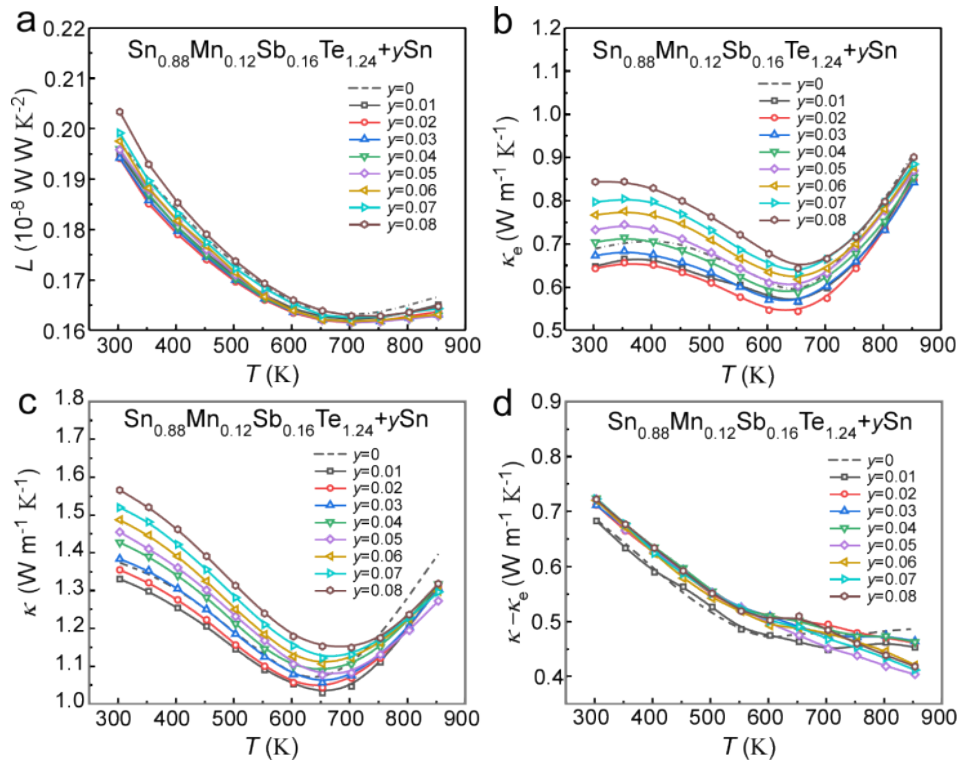
Fig. S15 Temperature-dependent (a) Lorenz number L, (b) electronic thermal conductivity κ_e, (c) total thermal conductivity κ, and (d) lattice thermal conductivity κ_l for $Sn_{0.88}Mn_{0.12}Sb_{0.16}Te_{1.24}+ySn$ (y=0-0.08) samples.
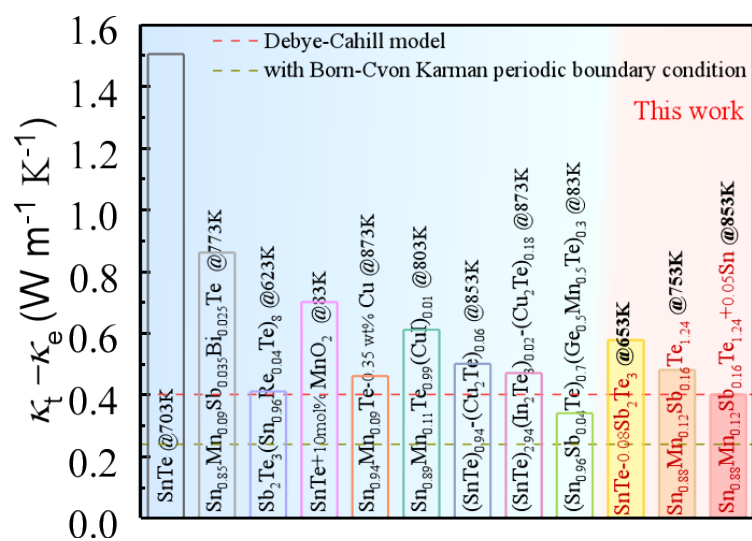
Fig. S16 Comparison of the exceptionally low thermal conductivity κ_l in this work with previously reported SnTe materials.[23-33]
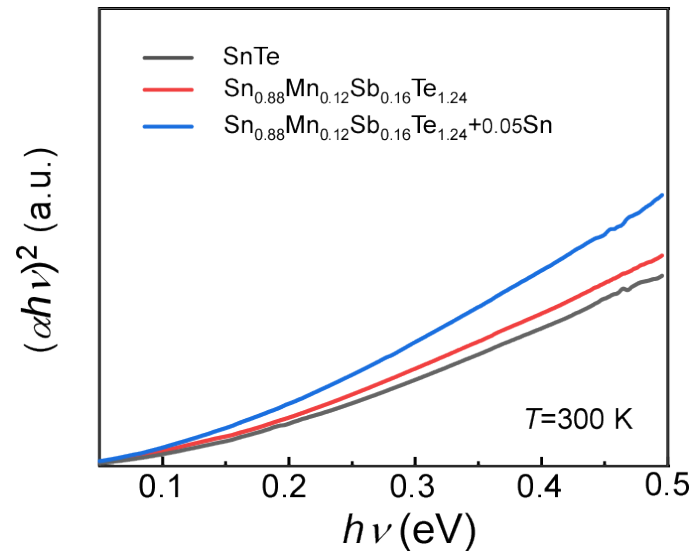
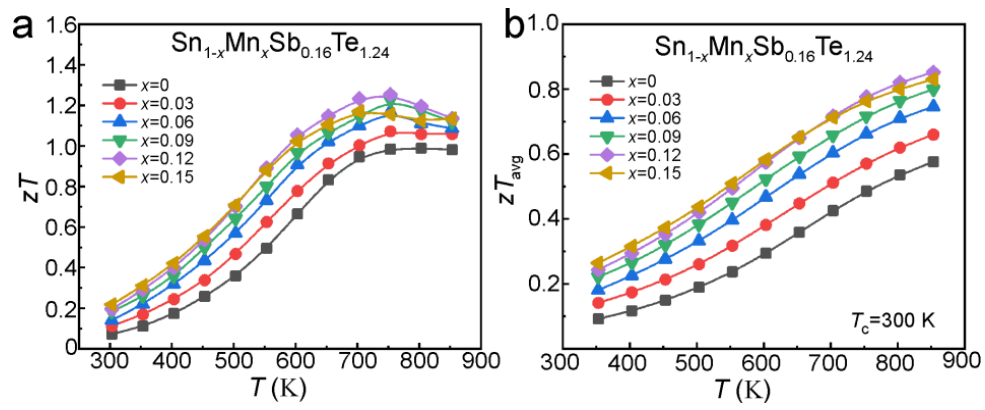**Fig. S17** Infrared absorption spectra of SnTe, $Sn_{0.88}Mn_{0.12}Sb_{0.16}Te_{1.24}$, and $Sn_{0.88}Mn_{0.12}Sb_{0.16}Te_{1.24}+0.05Sn$.

Fig. S18 Temperature-dependent figure of merit (a) zT and (b) average zT_{avg} for $Sn_{1-x}Mn_xSb_{0.16}Te_{1.24}$ (x=0-0.15) samples.
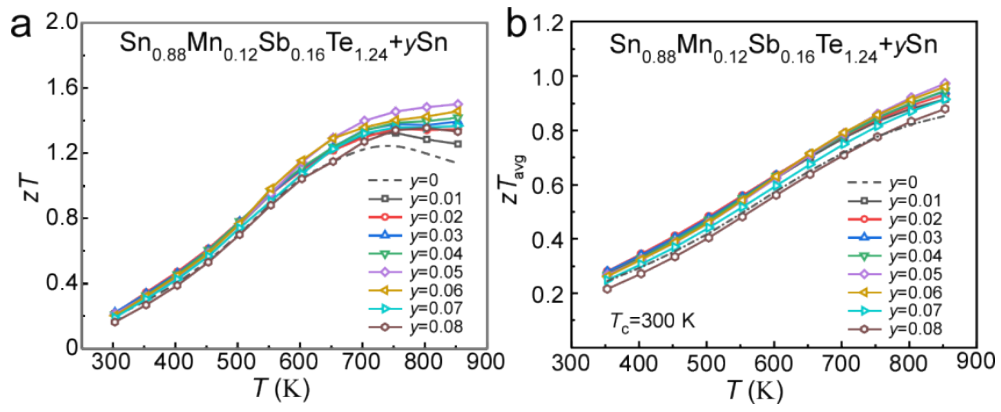
Fig. S19 Temperature-dependent figure of merit (a) zT and (b) average zT_{avg} for Sn$_{0.88}$Mn$_{0.12}$Sb$_{0.16}$Te$_{1.24}$+ySn (y=0-0.08) samples.
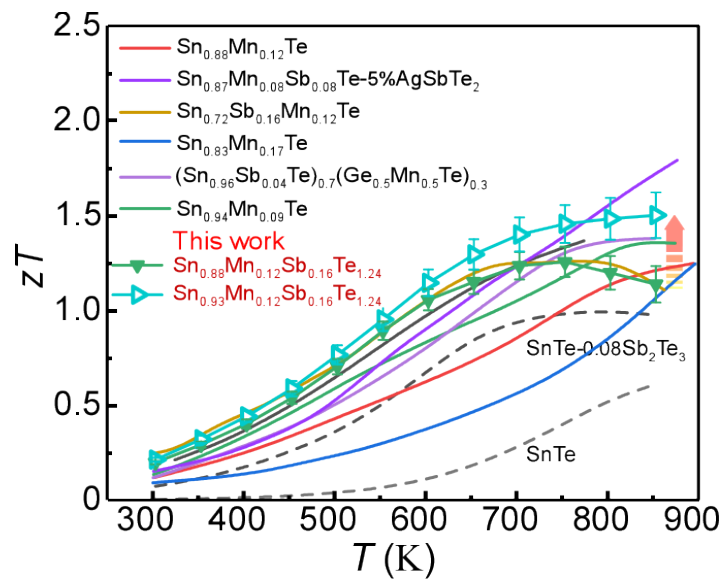
Fig. S20 Temperature-dependent zT in comparison with other reported SnTe materials.[29,31-33]
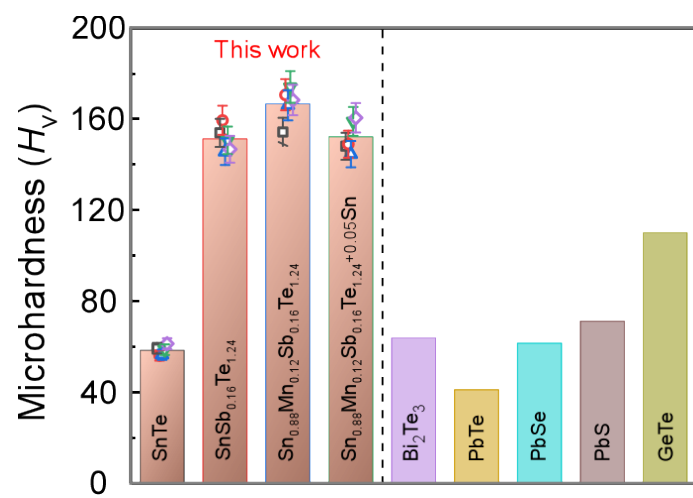
Fig. S21 Vickers hardness H_V of this work and comparison with other common thermoelectric candidates.[34]
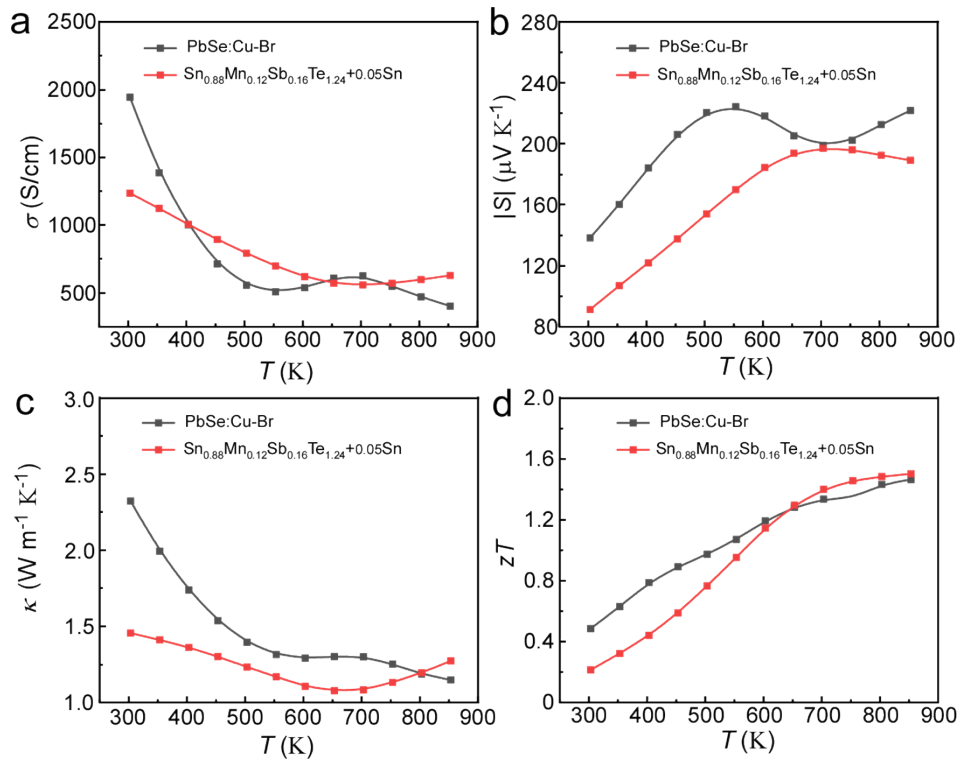
Fig. S22 (a) Temperature-dependent electrical conductivity σ, (b) Seebeck coefficient S, (c) total thermal conductivity κ, and (d) thermoelectric figure of merit zT for n-type PbSe and p-type SnTe materials.
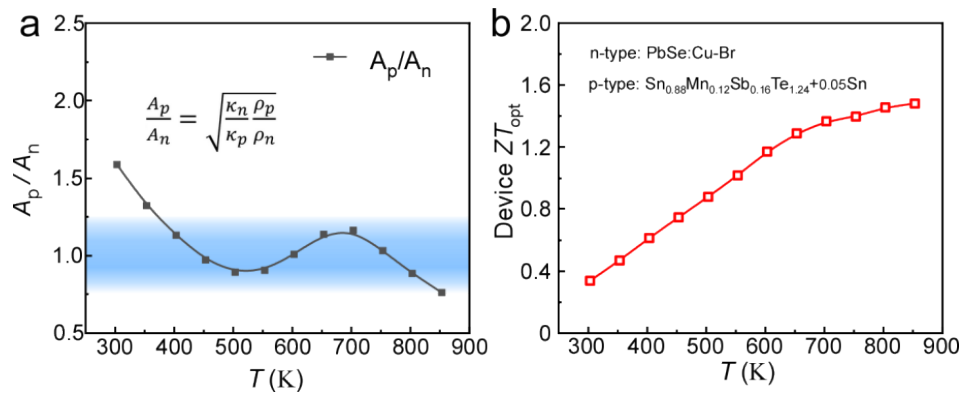
Fig. S23 (a) Cross-sectional area ratio of the *p*/*n* legs at the same height, and (b) optimal device thermoelectric figure of merit ZT_{opt} as a function of temperature for SnTe-PbSe-based thermoelectric materials.
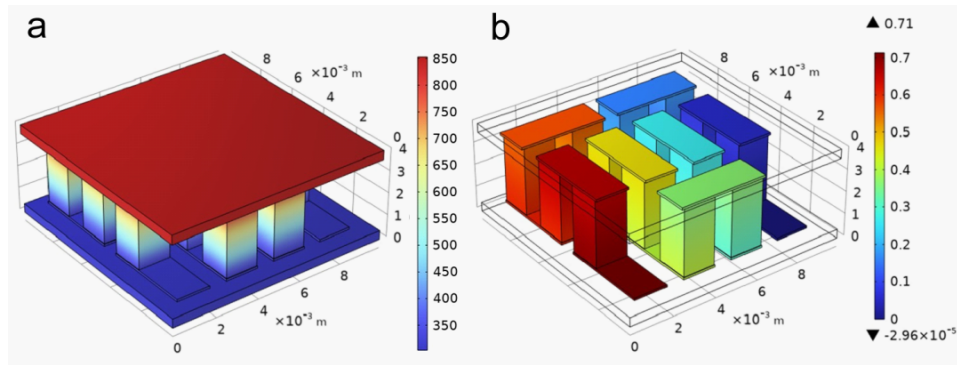
Fig. S24 (a) Temperature profile and (b) closed circuit voltages V of 7 pairs of p-type SnTe and n-type PbSe-based thermoelectric modules simulated by COMSOL. The cold end temperature of the thermoelectric module is 300 K, and the hot end temperature is 850 K, respectively.
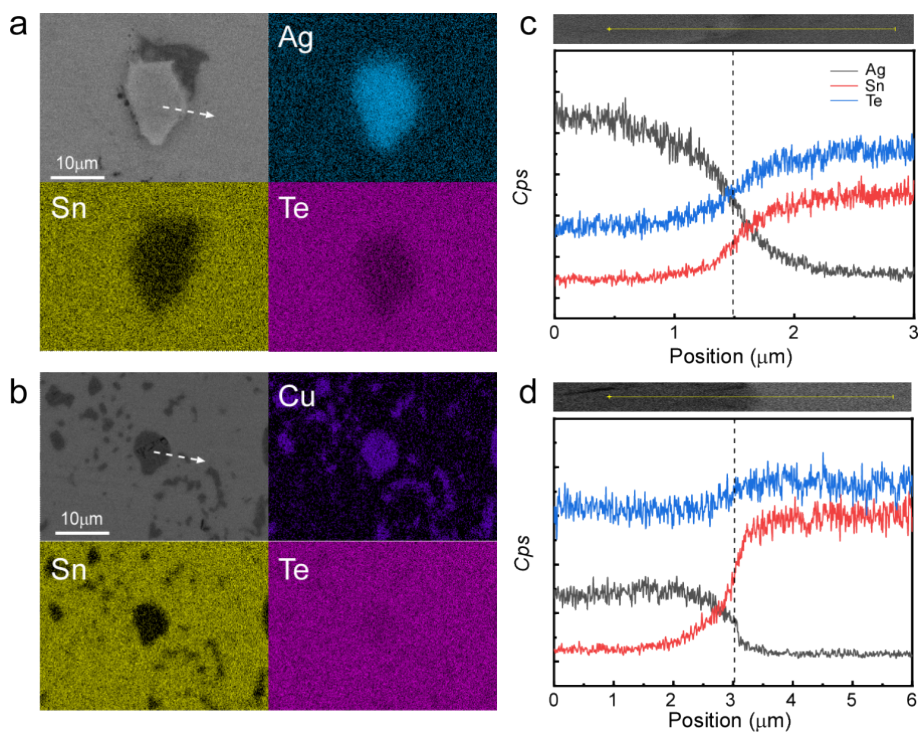
Fig. S25 Typical SEM images and EDS spectra of (a, c) Ag/SnTe and (b, d) Cu/SnTe interfaces after vacuum annealing at 850 K for 72 hours, including surface and line scans.
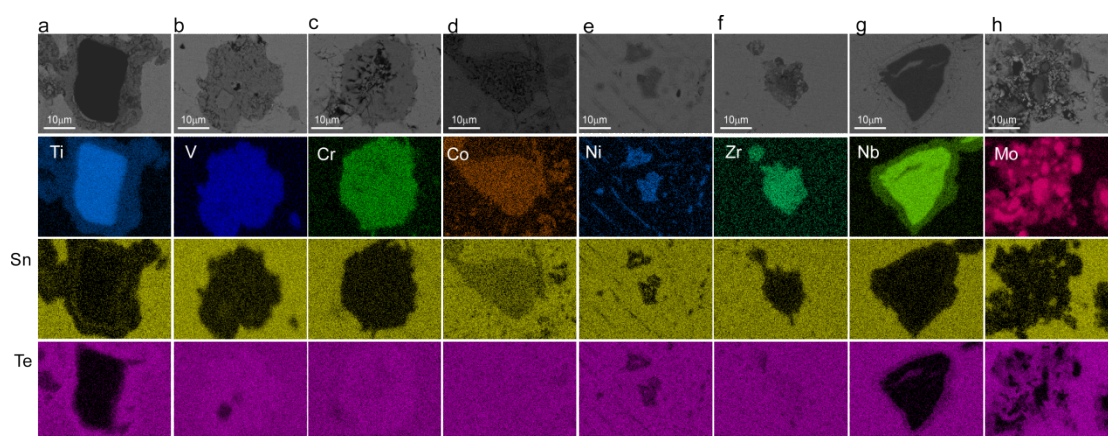
Fig. S26 SEM images and EDS mapping results of the interfaces between SnTe and eight types of metals after aging at 850 K for 72 hours: (a) Ti, (b) V, (c) Cr, (d) Co, (e) Ni, (f) Zr, (g) Nb, and (h) Mo.
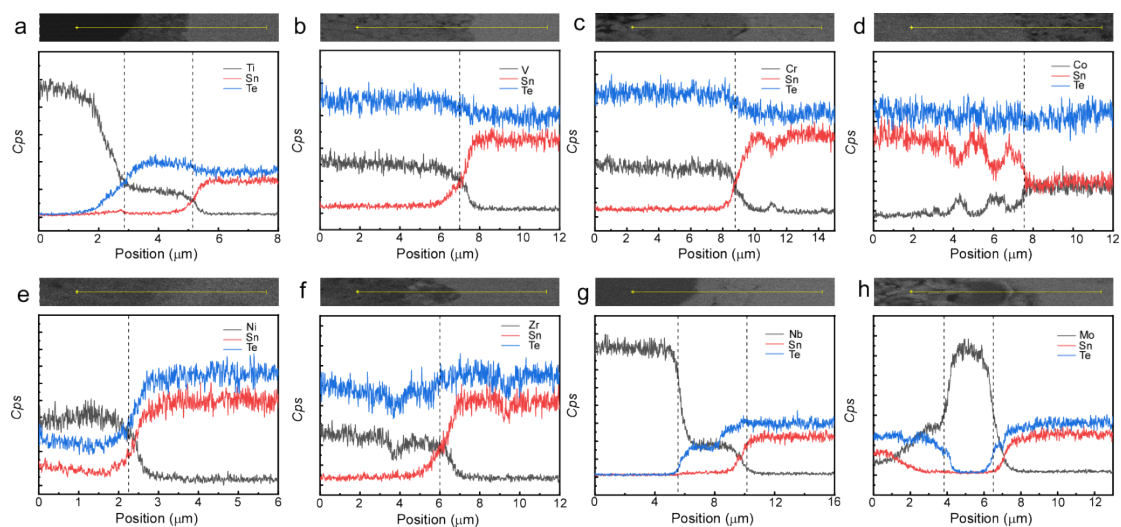
Fig. S27 EDS line scanning (along the direction indicated by the yellow solid line) of the reaction interfaces in the SnTe matrix after aging at 850 K for 72 hours: (a) Ti, (b) V, (c) Cr, (d) Co, (e) Ni, (f) Zr, (g) Nb, and (h) Mo.

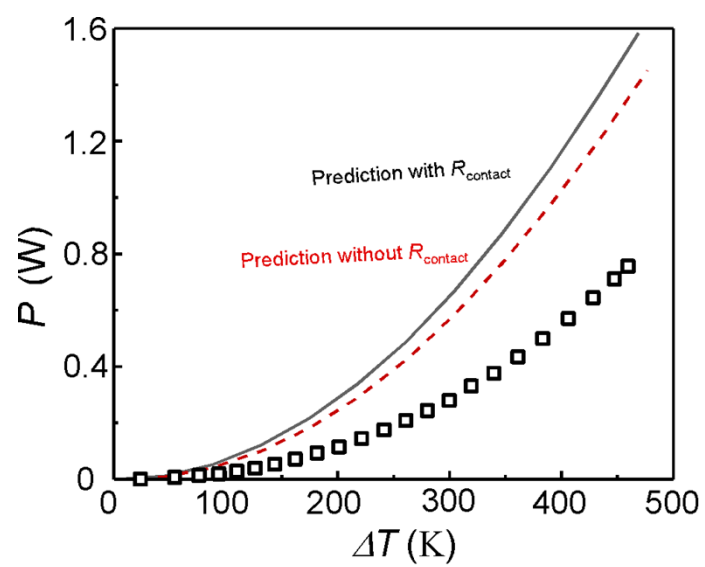**Fig. S28** Maximum output power of the module as a function of the temperature difference for *p*-SnTe/*n*-PbSe thermoelectric modules, along with a comparison to theoretical predictions.
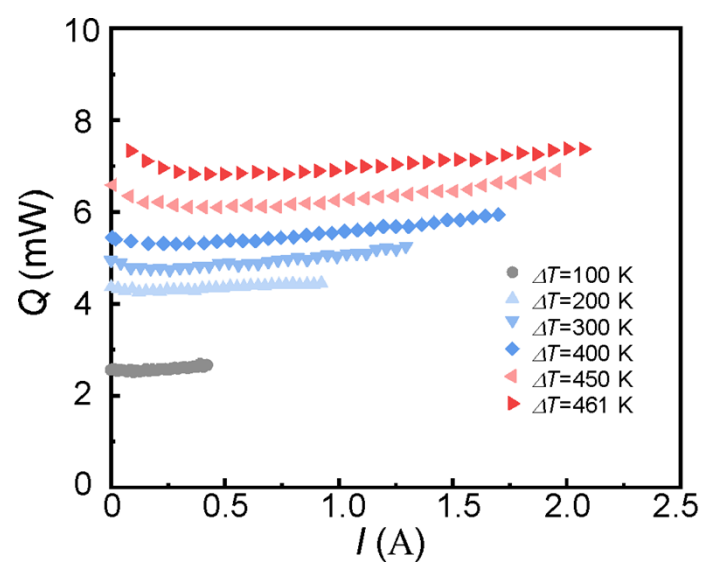
Fig. S29 Heat flow of the *p*-SnTe/*n*-PbSe thermoelectric module as a function of loop current.
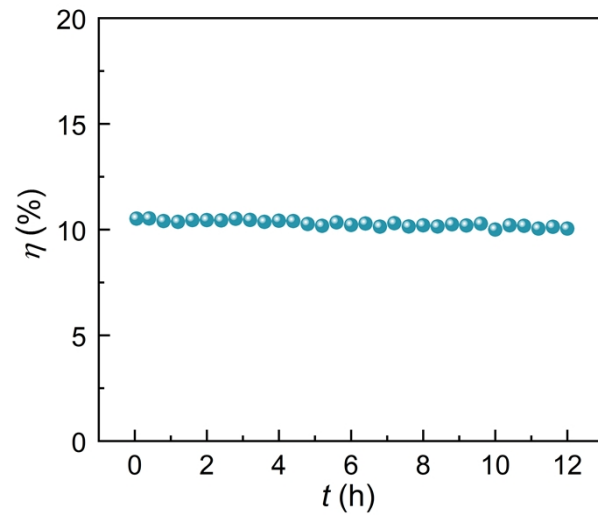
Fig. S30 Continuous measurement of the SnTe-based module at a temperature difference (ΔT) of 461 K.

Supplementary tables

Table S1 Density of $Sn_{0.88}Mn_{0.12}Sb_{0.16}Te_{1.24}$ and $Sn_{0.88}Mn_{0.12}Sb_{0.16}Te_{1.24}+0.05Sn$ samples in this work.

Composition	Measured density (g cm^{-3})	Relative density (%)
$SnSb_{0.16}Te_{1.24}$	6.257	97.491%
$Sn_{0.97}Mn_{0.03}Sb_{0.16}Te_{1.24}$	6.377	99.361%
$Sn_{0.94}Mn_{0.06}Sb_{0.16}Te_{1.24}$	6.370	99.252%
$Sn_{0.91}Mn_{0.09}Sb_{0.16}Te_{1.24}$	6.331	98.644%
$Sn_{0.88}Mn_{0.12}Sb_{0.16}Te_{1.24}$	6.33	98.629%
$Sn_{0.85}Mn_{0.15}Sb_{0.16}Te_{1.24}$	6.256	97.476%
$Sn_{0.88}Mn_{0.12}Sb_{0.16}Te_{1.24}+0.01Sn$	6.252	97.414%
$Sn_{0.88}Mn_{0.12}Sb_{0.16}Te_{1.24}+0.02Sn$	6.221	96.931%
$Sn_{0.88}Mn_{0.12}Sb_{0.16}Te_{1.24}+0.03Sn$	6.240	97.227%
$Sn_{0.88}Mn_{0.12}Sb_{0.16}Te_{1.24}+0.04Sn$	6.241	97.242%
$Sn_{0.88}Mn_{0.12}Sb_{0.16}Te_{1.24}+0.05Sn$	6.230	97.071%
$Sn_{0.88}Mn_{0.12}Sb_{0.16}Te_{1.24}+0.06Sn$	6.231	97.086%
$Sn_{0.88}Mn_{0.12}Sb_{0.16}Te_{1.24}+0.07Sn$	6.230	97.071%
$Sn_{0.88}Mn_{0.12}Sb_{0.16}Te_{1.24}+0.08Sn$	6.251	97.398%

Table S2 Parameters used to calculate carrier transport of SnTe based on the two band model.

Paramaters	Values
Combination of elastic constants C_l (Pa)	5.8×10^{10}
Ratio of the longitudinal to transverse band effective mass K_L	4 [4]
Ratio of the longitudinal to transverse band effective mass K_Σ	1 [4]
Band gap E_g (eV)	$0.054 + 4.2 \times 10^{-4} \times T$ [35]
Energy offset ΔE (eV)	$0.45 - 2.5 \times 10^{-4} \times T$ [8]
Band effective mass of V_L m_b^* (m_0)	$e^{lg0.17 + 0.5lg\frac{T}{300}}$
Band effective mass of V_Σ m_b^* (m_0)	1.92
Deformation potential of V_L E_{def} (eV)	35 (this work)
Deformation potential of V_Σ E_{def} (eV)	25 (this work)
Light valence Band degeneracy N_L	4
heavy valence Band degeneracy N_Σ	15

Table S3 Parameters adopted in the Debye-Callaway model simulation.

Parameters	Values
Longitudinal sound velocity v_L (m s^{-1})	3171[36]
Transverse sound velocity v_T (m s^{-1})	1220[36]
Sound velocity v (m s^{-1})	1967
Atomic mass Sn (kg)	1.97×10^{-25}
Atomic mass Te (kg)	2.12×10^{-25}
Atomic mass Sb (kg)	2.02×10^{-25}
Atomic mass Mn (kg)	9.13×10^{-26}
Atomic mass vacancy (kg)	0
Ionic radius Sn (Å)	0.93
Ionic radius Te (Å)	2.11
Ionic radius Sb (Å)	0.76
Ionic radius Mn (Å)	0.81
Ionic radius vacancy (Å)	50% $r_{Sn^{2+}}$
Grüneisen parameter γ	2.2[19,37,38]
Point defect scattering parameters Γ	(fitted)
Temperature-dependent ratio of normal phonon scattering to Umklapp scattering β	2.3 (fitted)

Table S4 Physical and chemical properties of Ti, V, Cr, Co, Ni, Zr, Nb, and Mo.

Metal	Ti	V	Cr	Co	Ni	Zr	Nb	Mo
Melting point (°C)	1668	1910	1907	1495	1455	1855	2477	2623
Resistivity ($\Omega \cdot m$)	6.5×10^{-7}	20.45	12.9	6.24×10^{-8}	6.84×10^{-6}	1.25×10^{-7}	1.6×10^{-7}	5.6
Thermal conductivity ($Wm^{-1}K^{-1}$)	14.63	0.307	0.94	0.01	90	16.5	0.537	138
Coefficient of expansion ($\times 10^{-6}\,K^{-1}$)	10.8	4.8	6.2	6.8	13	3.6	4.1	5.2

References:

1. R. Blachnik and R. Igel, *Z. Naturforsch. B*, 1974, **29**, 625-629.

2. Y. Pei, X. Shi, A. LaLonde, H. Wang, L. Chen and G. J. Snyder, *Nature*, 2011, **473**, 66-69.

3. H.-S. Kim, Z. M. Gibbs, Y. Tang, H. Wang and G. J. Snyder, *APL Mater.*, 2015, **3**, 041506.

4. M. Hong, Y. Wang, S. Xu, X. Shi, L. Chen, J. Zou and Z.-G. Chen, *Nano Energy*, 2019, **60**, 1-7.

5. W. H. Butler, *Phys. Rev. B*, 1985, **31**, 3260-3277.

6. H. Akai, *Journal of Physics-Condensed Matter*, 1989, **1**, 8045-8063.

7. V. L. Moruzzi, J. F. Janak and A. R. Williams, *Calculated electronic properties of metals*, 1978.

8. M. Zhou, Z. M. Gibbs, H. Wang, Y. Han, C. Xin, L. Li and G. J. Snyder, *Phys. Chem. Chem. Phys.*, 2014, **16**, 20741-20748.

9. Y. Xiao, H. Wu, W. Li, M. Yin, Y. Pei, Y. Zhang, L. Fu, Y. Chen, S. J. Pennycook, L. Huang, J. He and L.-D. Zhao, *J. Am. Chem. Soc.*, 2017, **139**, 18732-18738.

10. T. Seddon and S. C. Gupta, *Solid State Commun.*, 1976, **20**, 69-72.

11. C. Herring and E. Vogt, *Phys. Rev.*, 1956, **101**, 944-961.

12. Y. Pei, Z. M. Gibbs, A. Gloskovskii, B. Balke, W. G. Zeier and G. J. Snyder, *Adv. Energy Mater.*, 2014, **4**, 1400486.

13. Q. Zhang, B. Liao, Y. Lan, K. Lukas, W. Liu, K. Esfarjani, C. Opeil, D. Broido, G. Chen and Z. Ren, *Proc. Natl. Acad. Sci. U. S. A.*, 2013, **110**, 13261-13266.

14. Y. Pei, A. D. LaLonde, H. Wang and G. J. Snyder, *Energy Environ. Sci.*, 2012, **5**, 7963-6969.

15. L. M. Rogers, *J. Phys. D: Appl. Phys.*, 1968, **1**, 845-852.

16. J. Callaway and H. C. von Baeyer, *Phys. Rev.*, 1960, **120**, 1149-1154.

17. D. Bessas, I. Sergueev, H. C. Wille, J. Perßon, D. Ebling and R. P. Hermann, *Phys. Rev. B*, 2012, **86**.

18. J. Callaway, *Phys. Rev.*, 1959, **113**, 1046-1051.

19. H. Wang, T. Wang, J. Hwang, W. Su, H. Kim, J. Zhai, X. Wang, C. Wang and W.

Kim, *Inorg. Chem. Front.*, 2018, **5**, 793-801.

20. G. A. Slack, *Phys. Rev.*, 1957, **105**, 829-831.

21. B. Abeles, *Phys. Rev.*, 1963, **131**, 1906-1911.

22. Z. Bu, X. Zhang, Y. Hu, Z. Chen, S. Lin, W. Li, C. Xiao and Y. Pei, *Nat. Commun.*, 2022, **13**, 237.

23. S. K. Kihoi, H. Kim, H. Jeong, H. Kim, J. Ryu, S. Yi and H. S. Lee, *J. Alloys Compd.*, 2019, **806**, 361-369.

24. X. Xu, J. Cui, Y. Yu, B. Zhu, Y. Huang, L. Xie, D. Wu and J. He, *Energy Environ. Sci.*, 2020, **13**, 5135-5142.

25. Z. Zhou, J. Yang, Q. Jiang, J. Xin, S. Li, X. Wang, X. Lin, R. Chen, A. Basit and Q. Chen, *Chem. Mater.*, 2019, **31**, 3491-3497.

26. Z. Wang, L. Ding, L. Liu, Z. Tan, H. Pan, P. Jiang, W. Wu and Y. Yu, *Scr. Mater.*, 2023, DOI: 10.1016/j.scriptamat.2023.115315, 115315.

27. G. Wu, Z. Guo, Q. Zhang, X. Wang, L. Chen, X. Tan, P. Sun, G.-Q. Liu, B. Yu and J. Jiang, *J. Mater. Chem. A*, 2021, **9**, 13065-13070.

28. J. Tang, B. Gao, S. Lin, J. Li, Z. Chen, F. Xiong, W. Li, Y. Chen and Y. Pei, *Adv. Funct. Mater.*, 2018, **28**, 1803586-1803593.

29. Q. Zhang, R. Wang, K. Song, X. Tan, H. Hu, Z. Guo, G. Wu, P. Sun, G.-Q. Liu and J. Jiang, *Nano Energy*, 2022, **94**, 106940.

30. F. Guo, B. Cui, H. Geng, Y. Zhang, H. Wu, Q. Zhang, B. Yu, S. J. Pennycook, W. Cai and J. Sui, *Small*, 2019, **15**, e1902493.

31. G. Tan, F. Shi, S. Hao, H. Chi, T. P. Bailey, L. D. Zhao, C. Uher, C. Wolverton, V. P. Dravid and M. G. Kanatzidis, *J. Am. Chem. Soc.*, 2015, **137**, 11507-11522.

32. Y. Liu, X. Zhang, P. Nan, B. Zou, Q. Zhang, Y. Hou, S. Li, Y. Gong, Q. Liu, B. Ge, O. Cojocaru-Mirédin, Y. Yu, Y. Zhang, G. Chen, M. Wuttig and G. Tang, *Adv. Funct. Mater.*, 2022, **32**, 2209980.

33. X. Yan, S. Zheng, Z. Zhou, H. Wu, B. Zhang, Y. Huang, X. Lu, G. Han, G. Wang and X. Zhou, *Nano Energy*, 2021, **84**, 105879.

34. Q. Zhang, Z. Guo, R. Wang, X. Tan, K. Song, P. Sun, H. Hu, C. Cui, G. Q. Liu and J. Jiang, *Adv. Funct. Mater.*, 2022, **32**, 2205458.

35. G. Tan, L.-D. Zhao, F. Shi, J. W. Doak, S. H. Lo, H. Sun, C. Wolverton, V. P. Dravid, C. Uher and M. G. Kanatzidis, *J. Am. Chem. Soc.*, 2014, **136**, 7006-7017.

36. R. Moshwan, W. Liu, X. Shi, Y. Wang, J. Zou and Z.-G. Chen, *Nano Energy*, 2019, **65**, 104056.

37. R. Al Rahal Al Orabi, N. A. Mecholsky, J. Hwang, W. Kim, J.-S. Rhyee, D. Wee and M. Fornari, *Chem. Mater.*, 2015, **28**, 376-384.

38. C. Toher, J. J. Plata, O. Levy, M. de Jong, M. Asta, M. B. Nardelli and S. Curtarolo, *Phys. Rev. B*, 2014, **90**, 174107.